AGU PUBLICATIONS

Geophysical Research Letters

RESEARCH LETTER
10.1002/2015GL064845

Key Points:
- The whole Himalayan arc is locked to roughly 100 km width, with no resolvable aseismic patches
- GPS and geomorphic shortening rates are comparable, indicating an elastic geodetic surface strain
- The moment deficit builds up at a rate of $15.1 \pm 1 \times 10^{19}$ Nm/yr for the entire arc

Supporting Information:
- Tables S1 and S2, Figures S1–S7, and Captions for Data Sets S1–S3
- Data Set S1
- Data Set S2
- Table S3

Correspondence to:
V. L. Stevens,
vstevens@caltech.edu

Citation:
Stevens, V. L., and J. P. Avouac (2015), Interseismic coupling on the main Himalayan thrust, *Geophys. Res. Lett.*, *42*, 5828–5837, doi:10.1002/2015GL064845.

Received 8 JUN 2015
Accepted 8 JUL 2015
Accepted article online 14 JUL 2015
Published online 29 JUL 2015

Interseismic coupling on the main Himalayan thrust

V. L. Stevens[1] and J. P. Avouac[1,2]

[1]Geological and Planetary Sciences, California Institute of Technology, Pasadena, California, USA, [2]Bullard Laboratories, Cambridge University, Cambridge, UK

Abstract We determine the slip rate and pattern of interseismic coupling on the Main Himalayan Thrust along the entire Himalayan arc based on a compilation of geodetic, interferometric synthetic aperture radar, and microseismicity data. We show that convergence is perpendicular to the arc and increases eastwards from 13.3 ± 1.7 mm/yr to 21.2 ± 2.0 mm/yr. These rates are comparable to geological and geomorphic estimates, indicating an essentially elastic geodetic surface strain. The interseismic uplift rate predicted from the coupling model closely mimics the topography, suggesting that a small percentage of the interseismic strain is permanent. We find that the fault is fully locked along its complete length over about 100 km width. We don't find any resolvable aseismic barrier that could affect the seismic segmentation of the arc and limit the along-strike propagation of seismic ruptures. The moment deficit builds up at a rate of $15.1 \pm 1 \times 10^{19}$ N m/yr for the entire length of the Himalaya.

1. Introduction

There is now a relatively good coverage of GPS measurements of surface displacements spanning the Himalayan arc (Figures 1 and S1 in the supporting information). These data indicate that the Himalaya accommodates about half of the 40 mm/yr convergence rate between India and Eurasia as some earlier studies have shown [e.g., *Bilham et al.*, 1997; *Larson et al.*, 1999; *Jouanne et al.*, 2004]. The high strain rate is consistent with the high seismic hazard associated with the range. The Himalayan range has indeed produced a number of deadly earthquakes recently (e.g., M_w 7.8 Nepal 2015, M_w 6.9 Sikkim 2011, and M_w 7.6 Kashmir 2005) and has been known for even larger historical earthquakes of magnitude more than 8 (e.g., the M_w 8.5 [Assam 1950 *Chen and Molnar*, 1990] and the M_w 8.2 1934 Nepal-Bihar earthquakes [*Sapkota et al.*, 2013]), indicating that a fraction of the geodetic strain rate is elastic strain, which is ultimately released by earthquakes.

A primary objective of this study is to assess how much of the geodetic strain is actually elastic and to quantify the current rate of moment deficit accumulation along the Himalaya. This quantity is of importance as it sets the seismic hazard level [*Bilham et al.*, 2001]. We also aim to assess if this pattern is spatially stationary through time in the interseismic period, or whether it can vary significantly. To answer these questions, we adopt the same methodology as *Ader et al.* [2012], who focused on the Nepal Himalaya, but consider the entire Himalayan range based on a regional compilation of recent GPS, interferometric synthetic aperture radar (InSAR), and microseismicity data. As a starting point we assume that as demonstrated for the Himalaya of central Nepal, the long-term shortening rate across the range is entirely taken up by slip along the Main Himalayan Thrust (MHT) fault, the basal fault along which the Himlayan wedge is thrust over the Indian crust [e.g., *Cattin and Avouac*, 2000]. The geodetic data can then be used to determine both the long-term slip rate on the fault and the pattern of interseismic coupling. Interseismic coupling is defined as the ratio of interseismic deficit of slip rate to long-term slip rate (1 if the fault is fully locked and 0 if it is creeping at the long-term slip rate). The pattern of interseismic coupling can reveal locked patches where future earthquakes might occur, or aseismic barriers that can arrest earthquake ruptures, and allows us to calculate the rate of accumulation of moment deficit [*Chlieh et al.*, 2008; *Moreno et al.*, 2011; *Avouac*, 2015]. Hereafter, we first describe the data set and the method used. We next discuss the modeling results and implications.

2. Data

2.1. GPS

There has been a considerable amount of new GPS data from the Himalayan arc area published during the past few years. Coverage is irregular but now extends all the way along the Himalayan arc. We compiled the

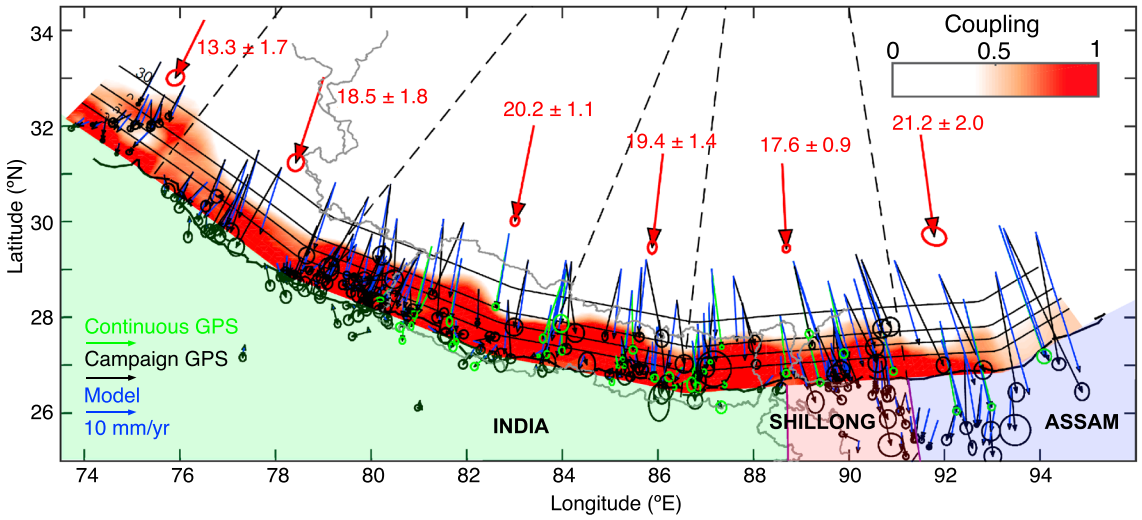

Figure 1. Coupling model and fit to the horizontal GPS data. The interseismic coupling is shown as shades of red. A coupling value of 1 means the area is fully locked, while a value of 0 means fully creeping. The green and black arrows and ellipses show the continuous and campaign GPS velocities (in the fixed-Indian reference frame of *Ader et al.* [2012]), with their error bars, respectively. The blue arrows are the modeled velocities, which fit with the coupling shown. The large red arrows show the long-term velocities in each region. The dashed black lines show the separation of the regions, within which the long-term velocity for that region is calculated, as shown by the large red arrows. The solid black lines, labeled at 10 km intervals, show the depth contours of the fault plane. The labels INDIA, SHILLONG, and ASSAM refer to three blocks which are assumed to be rigid. The residuals to the horizontal GPS, the InSAR, and leveling data are shown in Figure S5. Electronic data of the coupling pattern are included in a supporting information (SI) file.

GPS data from the literature [*Bettinelli et al.*, 2006; *Calais et al.*, 2006; *Socquet et al.*, 2006; *Gan et al.*, 2007; *Jade et al.*, 2007; *Banerjee et al.*, 2008; *Mukul et al.*, 2010; *Jade et al.*, 2011; *Ponraj et al.*, 2011; *Ader et al.*, 2012; *Mahesh et al.*, 2012; *Gahalaut et al.*, 2013; *Liang et al.*, 2013; *Schiffman et al.*, 2013; *Jade et al.*, 2014; *Kundu et al.*, 2014; *Vernant et al.*, 2014]. All the data were expressed in the same International Terrestrial Reference Frame 2005.

Where the GPS were highly spurious (e.g., where there were three measurements at one station, and one of the measurements greatly differed, or if the GPS velocity visually stuck out from the overall pattern), perhaps due to very local earthquakes , they were removed from the data set (see Data Set S1), or errors were doubled. The GPS were then converted into the fixed India reference frame using the pole of *Ader et al.* [2012]. The details of GPS processing can be found within the relevant papers. For the coupling model, 39 continuous stations and 174 campaign stations were used—those that were within 300 km of the fault trace (Figure S1). Measurements at the same location were averaged and weighted according to their uncertainties.

2.2. Leveling and InSAR Data

The pattern of coupling on a megathrust is better resolved where constraints from vertical displacements are available. Such constraints can be provided by leveling or InSAR measurements. We used leveling data from the Survey of Nepal collected between 1977 and 1990 [*Jackson and Bilham*, 1994]. The Survey followed a road through the Himalaya of central Nepal, and the location of the data can be seen in Figure S1. The uncertainties on the leveling data are low with respect to those on the GPS vertical and help constrain well the pattern of coupling locally [*Ader et al.*, 2012].

We used the InSAR data from a swath over the Kali Gandaki area in central Nepal [*Grandin et al.*, 2012] (Figure S1). The radar images were acquired between 2003 and 2010. The InSAR data were downsampled uniformly across the area by simply averaging nearby pixels to use 41 points in the inversion (Figure S1). These data, which were not used by *Ader et al.* [2012], improve the resolution significantly between 83°E and 84°E and from near the fault trace to 29°N.

2.3. Microseismicity

The background crustal seismicity in the Himalaya is known to consist mainly of thrust events in the area of stress buildup fringing the downdip end of the locked portion of the MHT [e.g., *Cattin and Avouac*, 2000; *Bollinger et al.*, 2004]. As such, these data can be used to help constrain interseismic coupling on the MHT. Within Nepal, earthquakes were taken from a relocated catalog of the National Seismological Centre (NSC), recorded between 1995 and 2001 ($0.8 < M < 5.5$) [*Ader et al.*, 2012; *Rajaure et al.*, 2013]. Between 77° and 81°E, seismicity from a second relocated catalog, recorded between April 2005 and June 2008, was used ($1 < M < 5$)

[*Mahesh et al.*, 2013]. Elsewhere, we used the NEIC catalog from 1964 to 2014 ($4 < M < 7.7$). Earthquakes from areas of active rifts in southern Tibet and events deeper than the Moho were removed from the catalogue so that only the crustal seismicity presumably associated to stress buildup on the MHT was kept.

2.4. Long-Term Shortening Rate Estimates on the MHT

The long-term shortening rate on the MHT has now been estimated at a number of locations along the Himalayan front from geomorphic and geological studies (Table S1). These data are used in this study for comparison to the long-term shortening rates on the MHT determined from the modeling of the geodetic data. In the Northwestern Himalaya, geomorphic studies of offset terraces give long-term shortening rates of 11–14 mm/yr [*Thakur et al.*, 2014; *Parkash et al.*, 2011; *Wesnousky et al.*, 1999]. In Nepal, geomorphic and structural studies give rates of 18–21 mm/yr [*Lavé and Avouac*, 2000; *Bollinger et al.*, 2014; *Mugnier et al.*, 2004]. At the eastern end of the Himlayan range, further geomorphic studies give similar shortening rates of 20–23 mm/yr [*Burgess et al.*, 2012; *Berthet et al.*, 2014].

3. Methods

We follow the method of *Ader et al.* [2012] but extend the model from just Nepal to the whole Himalayan range. As well as considering a larger area, an additional data set within Nepal (InSAR) and the wealth of GPS data now available elsewhere, we also modify the modeling technique to incorporate the microseismicity information. We invert the GPS, leveling, and InSAR data using the backslip approach [*Savage*, 1983] to solve for the long-term velocities and the pattern of coupling on the MHT. The slip deficit (which gives the pattern of coupling) and long-term slip rates computed from the Euler poles describing long-term block motions are summed together to model the GPS motions. The method assumes that interseismic surface strain is entirely elastic deformation driven by the pattern of creep on the MHT. This assumption is tested later by comparing GPS-derived horizontal shortening rate (calculated from the slip rate on the fault plane and its dip) with geomorphic/geological shortening rates.

We consider the total length of the arc, roughly 2000 km, from 73°E to 96°E. Due to the arcuate shape, we simplify the fault geometry (based on *Styron et al.* [2010]) into five planar subfaults (Figure S2). To allow for previously seen along-strike variations of the shortening rate across the range [e.g., *Jouanne et al.*, 2004; *Schiffman et al.*, 2013; *Vernant et al.*, 2014], we divide the arc into six different sections (Figure S2). We calculate the best fitting shortening rate within each of them. The boundaries of these sections were picked where the GPS appeared to change most and to coincide with the main extensional grabens in Southern Tibet and across the arc [*Gan et al.*, 2007; *Kundu et al.*, 2014; *Hurtado et al.*, 2001] (Figure S2). Slip on the MHT is allowed to happen in the strike-slip and dip-slip directions. We have taken the role of extension in a simplified way by assuming it is homogeneously distributed (as also assumed in *Ader et al.* [2012]).

The assumption of a rigid-Indian plate breaks down around the eastern end of the Himalayan arc where there is evidence for internal deformation [*Vernant et al.*, 2014]. To account for this deformation, we consider two blocks south of the eastern Himalaya (Figure 2), the easternmost one being the Assam block, and the other the Shillong block. The inversion solves for the poles of rotation of these two blocks with respect to India, as well as the long-term velocity on the MHT and the coupling pattern.

The fault is discretized into 2057 patches (17 downdip and 121 along strike, with dimensions roughly 15×17 km). The dip angle is set to 10° as in previous studies [*Ader et al.*, 2012; *Jouanne et al.*, 2004]. Note that the fault geometry is idealized as it does not need to present the real ramp-and-flats geometry of the fault where it is locked [*Vergne et al.*, 2001]. The elastostatic Green's functions relating unit slip on each patch to surface displacements at the data locations are computed using Okada's solution [*Okada*, 1985]. We assume an elastic half-space with Poisson coefficient of 0.25. The modeling is independent of the shear modulus. We take a value of 30 GPa to estimate moment from slip potency. The back slip azimuth is assumed equal to the azimuth of the long-term slip rate predicted by the Euler poles describing the rigid block motion of the various blocks. For each patch, the degree of interseismic coupling (i.e., locking) is found from the ratio of the slip deficit rate to the long-term slip rate. A value of 0 implies the fault patch is entirely creeping at the long-term slip rate, and a value of 1 implies that it is fully locked. Figure S2 shows the model setup.

We solve the equation

$$d = GM \tag{1}$$

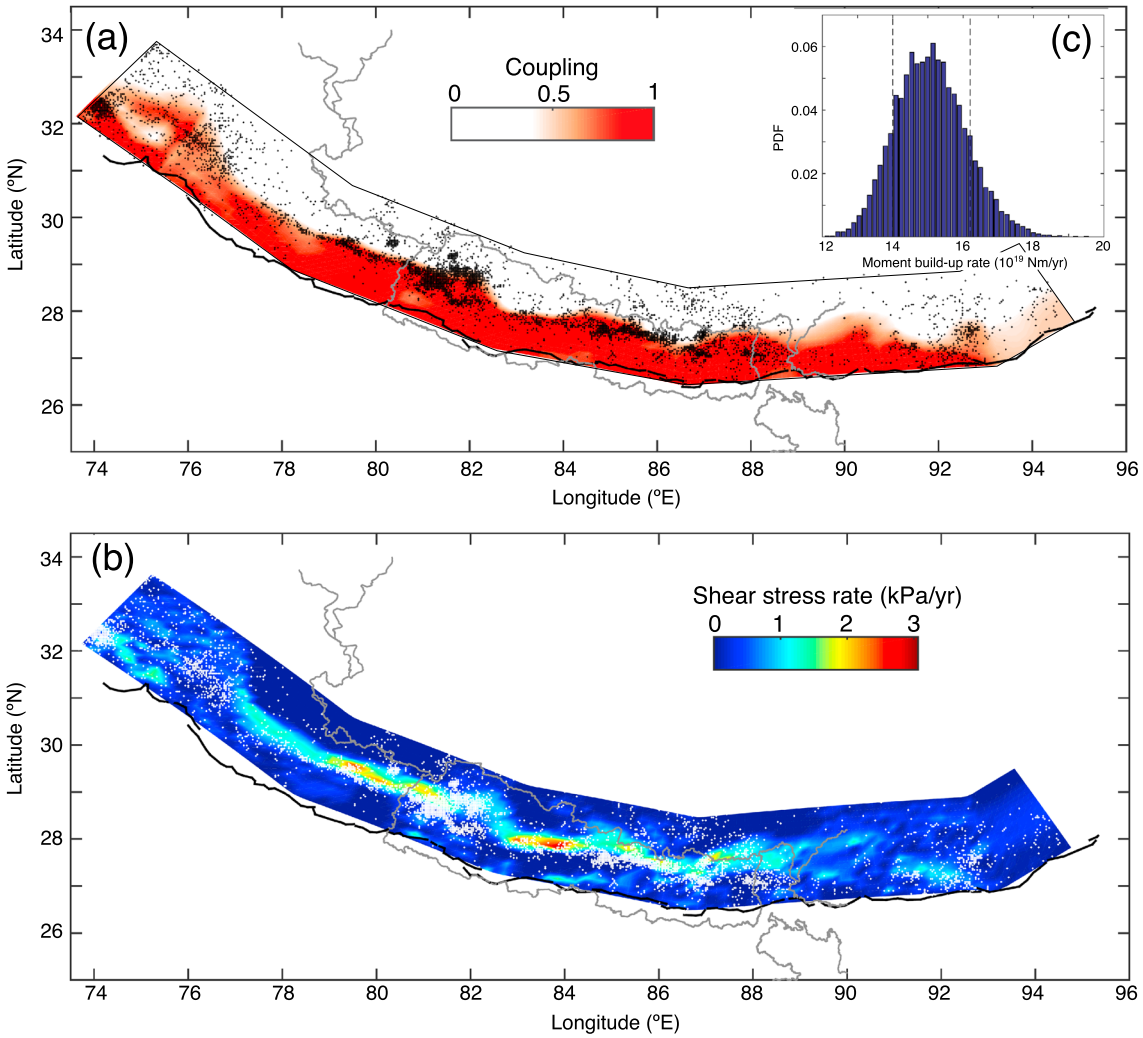

Figure 2. (a) The same coupling model as in Figure 1, with the location of seismicity used to regulate the Laplacian smoothing. Seismicity within Nepal is from an NSC catalog [*Ader et al.*, 2012; *Rajaure et al.*, 2013] seismicity between roughly 77°E and 81°E is from *Mahesh et al.* [2013], and the remainder is from NEIC. The modeled fault is outlined in black. (b) Shear stress accumulation rate on the fault plane, calculated from the coupling pattern, overlain by the same microseismicity as in Figure 2a, here shown as white dots. Electronic data of the stress rate pattern are included in an SI file. (c) Probability distribution function of the total moment buildup rate per year. Dashed lines show 1 standard deviation.

where d = data vector of 611 parameters, G = Green's function matrix (using *Okada* [1985]), and m = unknown parameters we want to solve for (slip rates on 2057 fault patches, long-term velocities in six sections and two poles of rotation (for each of the two eastern blocks)).

Because the inversion is ill posed, as the number of parameters exceeds the number of data points, we regularize the inversion by penalizing the roughness of the slip distribution. In practice, we minimize the Laplacian of the slip distribution. As in *Ader et al.* [2012], the weight put on the Laplacian is adjusted according to the resolution on each path, and 3 times stronger in the along-strike direction than downdip, as we expect there to be rapid variations along dip, but less rapid variations along strike. The resolution is calculated using the Moore-Penrose pseudoinverse matrix [*Aster et al.*, 2013]. We calculate the correlation of each patch with its neighbors and then weight each line of the Laplacian matrix by the decimal logarithm of the resolution size on the corresponding patch. The Laplacian is also regulated using the microseismicity information. We use the fact that microseismicity seems to follow areas with a large gradient of coupling (the downdip edge of the locked fault zone) where stress buildup is maximum [*Cattin and Avouac*, 2000; *Bollinger et al.*, 2004]. To encourage gradients of coupling to locate in areas of higher seismicity, the weighting on the Laplacian is reduced there. In practice the weight is inversely proportional to the number of events in that patch to the power of a third.

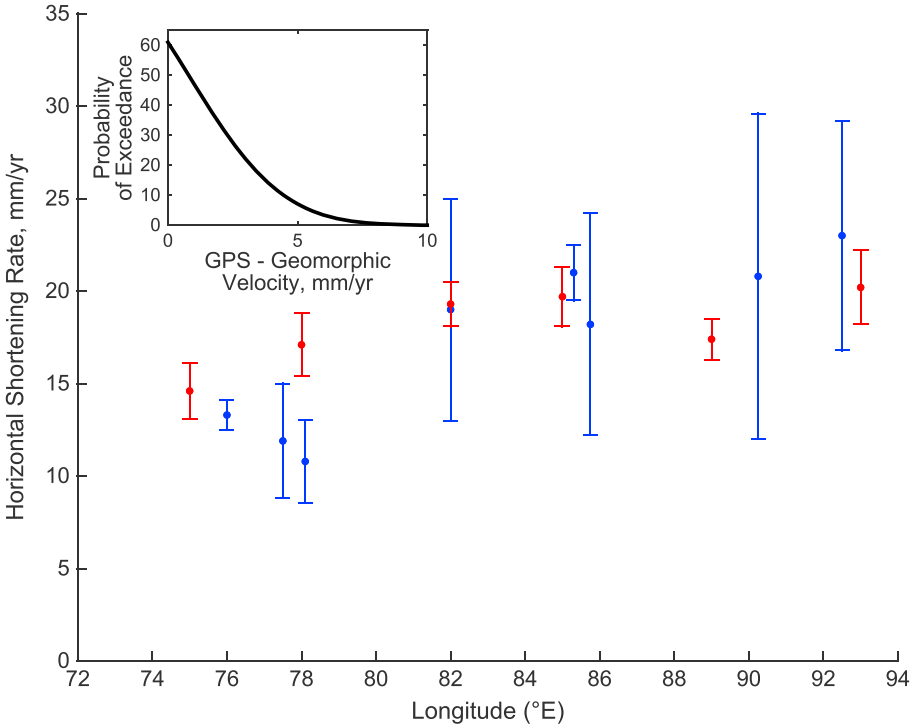

Figure 3. Shortening rate across the Himalayas from the results of this study (red) and geomorphic studies (blue). Geomorphic data from west to east are from *Thakur et al.* [2014], *Wesnousky et al.* [1999], *Parkash et al.* [2011], *Mugnier et al.* [2004], *Lavé and Avouac* [2000], *Bollinger et al.* [2014], *Berthet et al.* [2014], and *Burgess et al.* [2012]. Inset shows the probability that the average modeled long-term GPS velocities exceed the average velocities from geomorphic studies by different amounts.

The shape of the arc and extension in the Tibetan plateau causes a strike-slip component to appear at the downdip end of the modeled fault, 230–250 km north from the surface trace, which is an artifact of the model. To reduce this effect, we minimize the coupling at the downdip end, while elsewhere strike-slip motion is allowed freely.

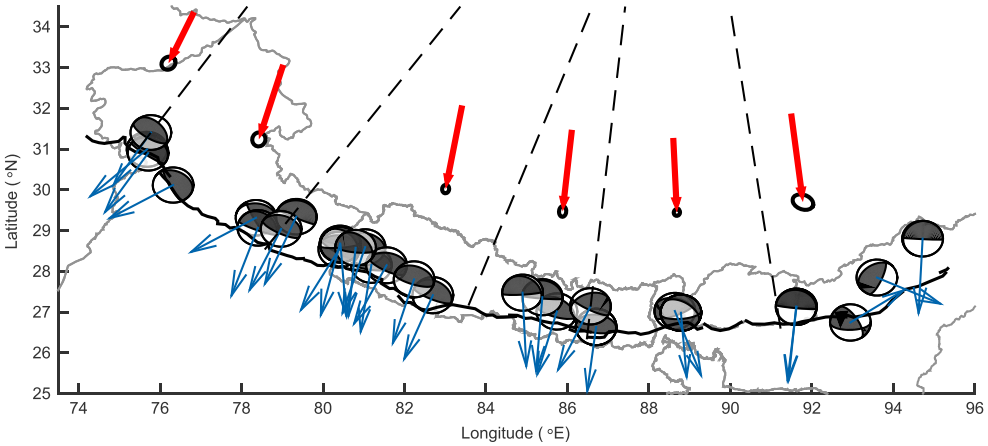

Figure 4. Focal mechanisms from the CMT catalog. Blue arrows show the direction of the slip vectors, i.e., the movement of the hanging wall. Red arrows show the direction of the long-term velocity vectors calculated in this study (in the fixed-Indian reference frame of *Ader et al.* [2012]). The dashed black lines show the boundaries between the different regions for which long-term velocities were calculated for. The thick black line shows the surface trace of the MHT, and the grey lines show country borders.

As in *Ader et al.* [2012] we determine the distribution of back slip on the fault by minimizing the chi-square criterion

$$\chi^2(\mathbf{m}) = \| \mathbf{C_d}^{-1/2}(\mathbf{Gm} - \mathbf{d}) \|_2 + \lambda \| \mathbf{\Lambda m} \|_2 + \mu \| \mathbf{I_d m} \|_2, \quad (2)$$

where $\mathbf{C_d}$ is the data covariance matrix, $\mathbf{\Lambda}$ is the Laplacian matrix, $\mathbf{I_d}$ is the matrix which gives the slip at depth when multiplied by $\mathbf{m}$, and λ and μ are weights on the constraints. We use $\lambda = 1.1$ and $\mu = 0.01$ to penalize the strike-slip component at depth, with $\mu = 0$ elsewhere than along the downdip end of the fault. The data sets are weighted equally, as the reduced chi-square calculated from the misfit between the observations and model prediction is similar for them all. After the inversion, we constrain the interseismic coupling value to lie between 0 and 1 by simply thresholding values above 1 and less than 0. Before the constraint, roughly 15% of the data lie outside of the permitted 0–1 range. Both the strike-slip and dip-slip components of each fault element and long-term velocities are used in the coupling calculation. We have not tested for the effect of earth sphericity, which we assume to be small as the strain signal is always dominated by local gradients of coupling. For a more detailed description of the method, see *Ader et al.* [2012].

4. Results and Discussion

4.1. The Coupling Pattern and Long-Term Shortening Rates

The pattern of coupling and long-term slip rates on the MHT corresponding to our best fitting model is shown in Figure 1. The reduced chi-square is 2.84, suggesting that some of the signal is not explained by the model's assumptions or that uncertainties are slightly underestimated. This model explains 92% of the data variance. Long-term velocities are found to be about 18–20 mm/yr across most of the arc, decreasing in the west to about 13 mm/yr (Figure 1).

The poles of rotation of the Assam and Shillong crustal blocks are listed in Table S2. The poles agree with those found by *Vernant et al.* [2014] for similar blocks, although the rotation rate for the Shillong block is about 50% lower in our solution. This may be due to the difference of block geometry or the trade-off with long-term velocities. Imposing the Euler poles of *Vernant et al.* [2014] does not alter the results significantly (Figure S3). The fit to the data changes depending on the regularization and the weight put on by the smoothing. Using the microseismicity to regulate the Laplacian, as in Figure 1, the reduced chi-square calculated from only the misfit between the observations and model prediction is 3.09, only 8% larger than the value of 2.84 obtained with a homogenous (though still weighted by data resolution) Laplacian. Figure S4 shows an inversion with the same parameters but not using the microseismicity to regulate the Laplacian. The difference between the two models is modest. The main difference is that where the sensitivity of the geodetic data is low, the downdip end of the locked fault zone in the model of Figure 1 coincides better with the zone of microseismic activity (Figure 2) than the model with homogeneous Laplacian weighting (Figure S4).

No systematic residuals are found (Figure S5), though larger residuals can be seen in the very east where the resolution is poorest (Figure S6). In places of low resolution, microseismicity helps in resolving the location of the downdip transition from locked to creeping.

The coupling pattern in Figure 1, the best fit to all the available data, shows that the fault is locked along its length to roughly 100 km downdip from the surface. The locking is nearly binary, as in there is a sharp transition between the locked and creeping zones. One exception is the very western end, where the fault appears to be locked to a much wider width, and the transition is more diffuse. This could be due to a more distributed zone of deformation in that part of the Himalaya [*Thakur et al.*, 2014] or the sparsity of GPS data. The lower coupling at the eastern end could be a reflection of lack of data in the area, and the complexity of local tectonics. Overall, the coupling pattern shows very little along-strike variation. This is much different from the heterogeneous pattern of coupling observed at subduction zones (see *Avouac* [2015], for a review), though similar to the findings of *Cheloni et al.* [2014] who find a uniform pattern of coupling along the southern front of the Alps.

The lack of creep, and the fairly homogenous coupling pattern in the 0–20 km seismogenic depth range, suggests that there are no obvious aseismic barriers that would arrest seismic ruptures.

Figure 2 confirms that background seismicity generally falls in the area of interseismic stress buildup. The correspondence is especially clear where the catalogs have been relocated, between about 77°E and 88°E. The correspondence of seismicity and the downdip edge of the locked zone has also been observed for the

southern front of the Alps [*Cheloni et al.*, 2014]. As expected, the model that does not use the seismicity to regulate the Laplacian does not have such quite good correlation, though it is still notable (Figure S4). Noteworthy is the fact that the relocated catalogue of *Mahesh et al.* [2013] which extends from 77°E and 81°E follows the downdip edge of the locked fall zone quite well also in the model of Figure S4 where we have not used the seismicity to weight the Laplacian smoothing. This observation confirms the correlation already noted for Nepal [*Cattin and Avouac*, 2000; *Bollinger et al.*, 2004; *Ader et al.*, 2012]. It is thus probably valid to assume that this correlation holds for the whole Himalayan arc. This suggests that if microseismicity elsewhere was better relocated, it would fall in a more compact area around the transition zone and help constrain better the coupling pattern.

4.2. Evidence That Interseismic Strain Is Primarily Elastic and Stationary

To test the assumption of elasticity, we compare estimates of long-term slip rates from geomorphic and structural studies to our geodetic estimates (Figure 3 and Table S1). The close correspondence suggests that most of the interseismic deformation is elastic. If a significant amount of deformation were permanent, the long-term convergence rate predicted by the geodetic data would be higher than the convergence rate found at the surface trace of the MHT. We see this happen outside of uncertainties only at one point, in the western Himalaya. This confirms the assumption that strain rate is elastic, geodetic convergence rates must vary little with time, and that anelastic strain of the upper crust in the interseismic period is small. Taking the geological and geodetic rates and associated uncertainties at face value, we can estimate the possible amount of geodetic shortening in excess of the geological rate that could reflect anelastic strain (Figure 3). After averaging the data, we find that the probability that anelastic interseimic convergence rate exceeds 2 mm/yr (hence about 10% of the geodetic shortening) is only 30%.

Figure 4 shows that the azimuth of slip during thrust events along the Himalayan arc is closely parallel to the azimuth of the long-term convergence determined from geodesy. This observation also indicates that interseismic strain is probably spatially stationary with time.

From the coupling pattern, the uplift rates can be calculated and then compared with the current topography (Figure 5). The close similarity in map view is striking, including detailed features such as the embayment of the arc at 82°E, and the kink in the western end. As was inferred earlier from the colocation of the bulge of interseismic uplift with the front of the High Himalaya [*Bilham et al.*, 1997; *Meade*, 2010], this correlation suggests that some fraction of the interseismic geodetic strain, albeit small as discussed above, is actually anelastic and contributes to topographic uplift in the long run. The main control on uplift rate might be the geometry of the MHT, rather than the precipitation pattern, as also concluded by *Godard et al.* [2006]. In fact, the building of the topography in the long term also probably result from ramp overthrusting [*Pandey et al.*, 1995; *Lavé and Avouac*, 2001; *Cattin and Avouac*, 2000; *Herman et al.*, 2010; *Grandin et al.*, 2012]. This mechanism cannot be assessed based on measurements of interseismic strain only, as if the ramp is within the locked domain it is undetectable. Only creeping patches, whether on the MHT or elsewhere, would contribute.

In the central Himalaya, where the coupling boundary is sharp, the uplift rate change is sharp, and this corresponds well with the steep topographic front. This downdip variation of coupling is possibly of thermal origin. The transition zone between locked and creeping coincides approximately with where the MHT intersects the 350°C isotherm (determined by *Herman et al.* [2010]). Slip is expected to be stable at higher temperature for quartzofeldspathic rocks based on laboratory measurements [*Blanpied et al.*, 1995]. Fluids released from metamorphic reactions could also play a role in favoring the transition to aseismic creep [*Avouac*, 2003]. In the east and the west, the coupling change occurs over a greater downdip distance, which reflects in the modeled uplift rate, and this is also seen in the topography. See Figure S7 for cross sections of the modeled uplift rate and topography. The close correlation of interseismic uplift with topography is another indication that the coupling pattern is probably stationary through time.

4.3. Seismic Moment Buildup Rate

The long-term velocities and coupling pattern can be used to calculate the seismic moment buildup rate. Here we adopt the conservative hypothesis that all of the interseismic surface strain is elastic. This can be seen in Figure 2c, with a most likely rate of $15.1 \pm 1.1 \times 10^{19}$ N m/yr. This quantity is estimated from the area of the fault plane and the calculated slip on each patch. The standard deviation (shown as dashed black lines on Figure 2c) is estimated by Monte Carlo simulation of 10,000 different distributions of patch velocities, calculated from the best fitting patch velocity, the covariance matrix and the chi squared fit.

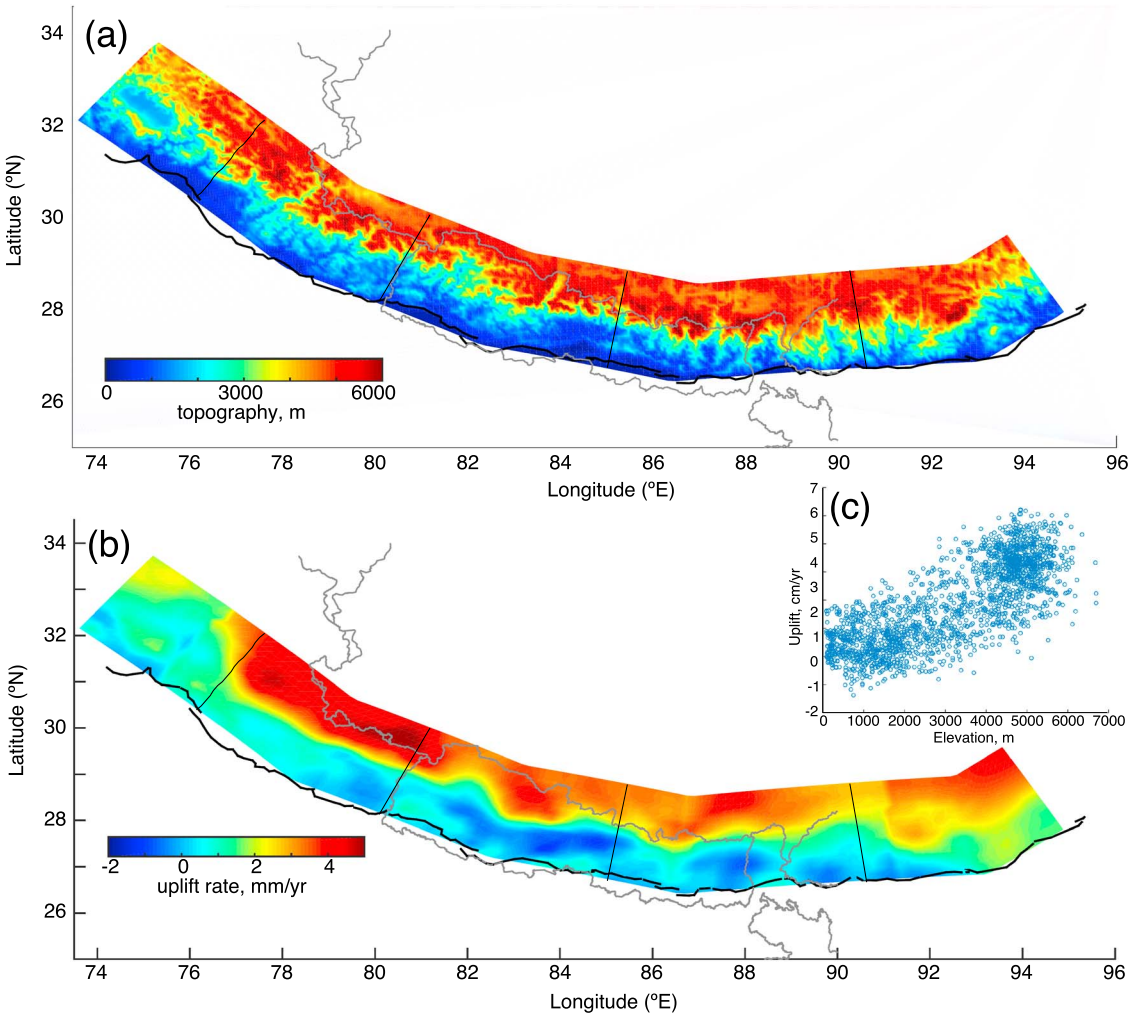

Figure 5. Comparison of topography with uplift rate. (a) Topography. Black lines show location of topographic and uplift rate profiles shown in Figure S7. (b) Uplift rates calculated from the coupling pattern. (c) Correlation of topography with uplift rate, *R* value 0.78.

5. Conclusions

All along the Himalayan arc the MHT appears to be fairly uniformly locked from the surface to beneath the front of the high range over a width of 100 ± 20 km, except in the far west where it extends to about 150 km. We see only modest variations of the geometry of the lower edge of the locked zone, which also reflects in the seismicity and topography. We see no resolvable aseismic barriers that could affect seismic ruptures, so if the seismic activity of the Himalaya is segmented, the cause for the segmentation would have to be of another origin. We can imagine an earthquake nucleating at any point along the arc and rupturing for a significant distance. In this context, zones of lower stress due to past earthquakes or geometric complexities would be the main factors contributing to the arrest of seismic ruptures along strike.

The amount of anelastic deformation in the interseismic period has to be small given the consistency of geodetic slip rate on the MHT calculated here, with range front velocities determined from geological studies; the creep rate at depth is transferred to the surface trace of the fault requiring interseismic deformation of the overhanging thrust sheet to be mostly recovered during slip events on the locked portion of the MHT. However, because of the correlation between interseismic uplift rates and the topography, the anelastic deformation cannot be null. From the general agreement between geodetic and geological rates, we find the fraction of anelastic deformation is up to 10% at the 70% confidence level.

The variations of the downdip edge of the locked zone are consistent with geodesy, seismicity, and topography. Evidence for the stationarity of slip rates and interseismic coupling through time comes from three

sources: (1) the correlation of geomorphic and GPS studies, (2) the correspondence of topography and uplift, and (3) the consistency of earthquake thrust vectors with GPS velocities. This study provides constraints on the rate of accumulation of seismic moment which needs to be released by transient slip events on the MHT. The results from this study can be used to constrain the probable location, frequency, and magnitude of large earthquakes in the Himalaya based on a slip budget approach. This analysis is left for a subsequent study.

Acknowledgments
The GPS used for the inversion are included in a SI file. The coupling and stress rate maps are provided as electronic data in SI files. All data for this paper are properly cited and referred to in the reference list. Jack Loveless and an anonymous reviewer gave useful reviews and comments.

The Editor thanks John Loveless and an anonymous reviewer for their assistance in evaluating this paper.

References

Ader, T., et al. (2012), Convergence rate across the Nepal Himalaya and interseismic coupling on the Main Himalayan Thrust: Implications for seismic hazard, *J. Geophys. Res.*, *117*, B04403, doi:10.1029/2011JB009071.

Aster, R. C., B. Borchers, and C. H. Thurber (2013), Parameter estimation and inverse problems, second ed.

Avouac, J. P. (2003), Mountain building, erosion and the seismic cycle in the Himalaya, in *Advances in Geophysics*, vol. 46, Elsevier, San Diego, Calif., doi:10.1016/S0065-2687(03)46001-9

Avouac, J.-P. (2015), From geodetic imaging of seismic and aseismic fault slip to dynamic modeling of the seismic cycle, *Ann. Rev. Earth Planet. Sci.*, *43*(1), 233–271, doi:10.1146/annurev-earth-060614-105302.

Banerjee, P., R. Bürgmann, B. Nagarajan, and E. Apel (2008), Intraplate deformation of the Indian subcontinent, *Geophys. Res. Lett.*, *35*, L18301, doi:10.1029/2008GL035468.

Berthet, T., J.-F. Ritz, M. Ferry, P. Pelgay, R. Cattin, D. Drukpa, R. Braucher, and G. Hetényi (2014), Active tectonics of the Eastern Himalaya: New constraints from the first tectonic geomorphology study in Southern Bhutan, *Geology*, *42*(5), 427–430, doi:10.1130/G35162.1.

Bettinelli, P., J.-P. Avouac, M. Flouzat, F. Jouanne, L. Bollinger, P. Willis, and G. Chitrakar (2006), Plate motion of India and interseismic strain in the Nepal Himalaya from GPS and DORIS measurements, *J. Geod.*, *80*(8-11), 567–589, doi:10.1007/s00190-006-0030-3.

Bilham, R., K. Larson, and J. Freymueller (1997), GPS measurements of present-day convergence across the Nepal Himalaya, *Nature*, *386*, 61–64.

Bilham, R., V. K. Gaur, and P. Molnar (2001), Himalayan seismic hazard, *Science*, *293*(5534), 1442–1444, doi:10.1126/science.1062584.

Blanpied, M. L., D. A. Lockner, and J. D. Byerlee (1995), Frictional slip of granite at hydrothermal conditions, *J. Geophys. Res.*, *100*(B7), 13,045–13,064, doi:10.1029/95JB00862.

Bollinger, L., J. P. Avouac, R. Cattin, and M. R. Pandey (2004), Stress buildup in the Himalaya, *J. Geophys. Res.*, *109*, B11405, doi:10.1029/2003JB002911.

Bollinger, L., S. N. Sapkota, P. Tapponnier, Y. Klinger, M. Rizza, J. Van der Woerd, D. R. Tiwari, R. Pandey, A. Bitri, and S. Bes de Berc (2014), Estimating the return times of Great Himalayan earthquakes in Eastern Nepal: Evidence from the Patu and Bardibas strands of the Main Frontal Thrust, *J. Geophys. Res. Solid Earth*, *119*, 7123–7163, doi:10.1002/2014JB010970.

Burgess, W. P., A. Yin, C. S. Dubey, Z.-K. Shen, and T. K. Kelty (2012), Holocene shortening across the Main Frontal Thrust Zone in the Eastern Himalaya, *Earth Planet. Sci. Lett.*, *357-358*, 152–167, doi:10.1016/j.epsl.2012.09.040.

Calais, E., L. Dong, M. Wang, Z. Shen, and M. Vergnolle (2006), Continental deformation in Asia from a combined GPS solution, *Geophys. Res. Lett.*, *33*, L24319, doi:10.1029/2006GL028433.

Cattin, R., and J. P. Avouac (2000), Modeling mountain building and the seismic cycle in the Himalaya of Nepal, *J. Geophys. Res.*, *105*(B6), 13,389–13,407, doi:10.1029/2000JB900032.

Cheloni, B., N. D'Agostino, and G. Selvaggi (2014), Interseismic coupling, seismic potential, and earthquake recurrence on the southern front of the Eastern Alps (NE Italy), *J. Geophys. Res. Solid Earth*, *119*, 4448–4468, doi:10.1002/2014JB010954.

Chen, W.-P., and P. Molnar (1990), Source parameters of earthquakes and intraplate deformation beneath the Shillong Plateau and the Northern Indoburman ranges, *J. Geophys. Res.*, *95*(B8), 12,527–12,552, doi:10.1029/JB095iB08p12527.

Chlieh, M., J. P. Avouac, K. Sieh, D. H. Natawidjaja, and J. Galetzka (2008), Heterogeneous coupling of the Sumatran Megathrust constrained by geodetic and paleogeodetic measurements, *J. Geophys. Res.*, *113*, B05305, doi:10.1029/2007JB004981.

Gahalaut, V. K., et al. (2013), Aseismic plate boundary in the Indo-Burmese wedge, Northwest Sunda arc, *Geology*, *41*, 235–238, doi:10.1130/G33771.1.

Gan, W., P. Zhang, Z.-K. Shen, Z. Niu, M. Wang, Y. Wan, D. Zhou, and J. Cheng (2007), Present-day crustal motion within the Tibetan Plateau inferred from GPS measurements, *J. Geophys. Res.*, *112*, B08416, doi:10.1029/2005JB004120.

Godard, V., J. Lavé, and R. Cattin (2006), *Numerical modelling of erosion processes in the Himalayas of Nepal: Effects of spatial variations of rock strength and precipitation*, vol. 253, pp. 341–358, Geol. Soc., Spec. Publ., London, U. K., doi:10.1144/GSL.SP.2006.253.01.18.

Grandin, R., M.-P. Doin, L. Bollinger, B. Pinel-Puysségur, G. Ducret, R. Jolivet, and S. N. Sapkota (2012), Long-term growth of the Himalaya inferred from interseismic InSAR measurement, *Geology*, *40*, 1059–1062, doi:10.1130/G33154.1.

Herman, F., et al. (2010), Exhumation, crustal deformation, and thermal structure of the Nepal Himalaya derived from the inversion of thermochronological and thermobarometric data and modeling of the topography, *J. Geophys. Res.*, *115*, B06407, doi:10.1029/2008JB006126.

Hurtado, J. M., K. V. Hodges, and K. X. Whipple (2001), Neotectonics of the Thakkhola Graben and implications for recent activity on the South Tibetan fault system in the central Nepal Himalaya, *Geol. Soc. Am. Bull.*, *113*(2), 222–240.

Jackson, M., and R. Bilham (1994), Constraints on Himalayan deformation inferred from vertical velocity fields in Nepal and Tibet, *J. Geophys. Res.*, *99*(B7), 13,897–13,912, doi:10.1029/94JB00714.

Jade, S., et al. (2007), Estimates of interseismic deformation in Northeast India from GPS measurements, *Earth Planet. Sci. Lett.*, *263*(3–4), 221–234, doi:10.1016/j.epsl.2007.08.031.

Jade, S., H. Raghavendra Rao, M. Vijayan, V. Gaur, B. Bhatt, K. Kumar, S. Jaganathan, M. Ananda, and P. Dileep Kumar (2011), GPS-derived deformation rates in Northwestern Himalaya and Ladakh, *Int. J. Earth Sci.*, *100*(6), 1293–1301, doi:10.1007/s00531-010-0532-3.

Jade, S., et al. (2014), Contemporary deformation in the Kashmir-Himachal, Garhwal and Kumaon Himalaya: Significant insights from 1995-2008 GPS time series, *J. Geod.*, *88*(6), 539–557, doi:10.1007/s00190-014-0702-3.

Jouanne, F., J. L. Mugnier, J. F. Gamond, P. Le Fort, M. R. Pandey, L. Bollinger, M. Flouzat, and J. P. Avouac (2004), Current shortening across the Himalayas of Nepal, *Geophys. J. Int.*, *157*(1), 1–14, doi:10.1111/j.1365-246X.2004.02180.x.

Kundu, B., R. K. Yadav, B. S. Bali, S. Chowdhury, and V. K. Gahalaut (2014), Oblique convergence and slip partitioning in the NW Himalaya: Implications from GPS measurements, *Tectonics*, *33*(10), 2013–2024, doi:10.1002/2014TC003633.

Larson, K. M., R. Bürgmann, R. Bilham, and J. T. Freymueller (1999), Kinematics of the India-Eurasia collision zone from GPS measurements, *J. Geophys. Res.*, *104*(B1), 1077–1093, doi:10.1029/1998JB900043.

Lavé, J., and J. P. Avouac (2000), Active folding of fluvial terraces across the Siwaliks Hills, Himalayas of central Nepal, *J. Geophys. Res.*, *105*(B3), 5735–5770, doi:10.1029/1999JB900292.

Lavé, J., and J. P. Avouac (2001), Fluvial incision and tectonic uplift across the Himalayas of central Nepal, *J. Geophys. Res.*, *106*(B11), 26,561–26,591.

Liang, S., W. Gan, C. Shen, G. Xiao, J. Liu, W. Chen, X. Ding, and D. Zhou (2013), Three-dimensional velocity field of present-day crustal motion of the Tibetan Plateau derived from GPS measurements, *J. Geophys. Res. Solid Earth*, *118*, 5722–5732, doi:10.1002/2013JB010503.

Mahesh, P., et al. (2012), Rigid Indian plate: Constraints from GPS measurements, *Gondwana Res.*, *22*(34), 1068–1072, doi:10.1016/j.gr.2012.01.011.

Mahesh, P., S. S. Rai, K. Sivaram, A. Paul, S. Gupta, R. Sarma, and V. K. Gaur (2013), One-dimensional reference velocity model and precise locations of earthquake hypocenters in the Kumaon-Garhwal Himalaya, *Bull. Seismol. Soc. Am.*, *103*(1), 328–339, doi:10.1785/0120110328.

Meade, B. J. (2010), The signature of an unbalanced earthquake cycle in Himalayan topography?, *Geology*, *38*(11), 987–990, doi:10.1130/G31439.1.

Moreno, M., et al. (2011), Heterogeneous plate locking in the SouthŰcentral Chile subduction zone: Building up the next great earthquake, *Earth Planet. Sci. Lett.*, *305*(34), 413–424, doi:10.1016/j.epsl.2011.03.025.

Mugnier, J., P. Huyghe, P. Leturmy, and F. Jouanne (2004), Episodicity and rates of thrust-sheet motion in the Himalayas (Western Nepal), in *Thrust Tectonics and Hydrocarbon System*, vol. 82, pp. 91–114, AAPG Memoir. [Available at http://archives.datapages.com/data/specpubs/memoir82/CHAPTER6/CHAPTER6.HTM.]

Mukul, M., S. Jade, A. Bhattacharyya, and K. Bhusan (2010), Crustal shortening in convergent orogens: Insights from Global Positioning System (GPS) measurements in Northeast India, *J. Geol. Soc. India*, *75*(1), 302–312, doi:10.1007/s12594-010-0017-9.

Okada, Y. (1985), Surface deformation due to shear and tensile faults in a half-space, *Bull. Seismol. Soc. Am.*, *75*(4), 1135–1154.

Pandey, M. R., R. P. Tandukar, J. P. Avouac, J. Lavé, and J. P. Massot (1995), Interseismic strain accumulation on the Himalayan crustal ramp (Nepal), *Geophys. Res. Lett.*, *22*(7), 751–754, doi:10.1029/94GL02971.

Parkash, B., R. Rathor, P. Pati, R. Jakhmola, and S. Singh (2011), Convergence rates along the Himalayan Frontal Thrust inferred from terraces at Chandidevi Temple hill, Hardwar, Northwestern Himalaya, *Curr. Sci.*, *100*, 1426–1432.

Ponraj, M., S. Miura, C. D. Reddy, S. Amirtharaj, and S. H. Mahajan (2011), Slip distribution beneath the central and Western Himalaya inferred from GPS observations, *Geophys. J. Int.*, *185*(2), 724–736, doi:10.1111/j.1365-246X.2011.04958.x.

Rajaure, S., S. N. Sapkota, L. B. Adhikari, B. Koirala, M. Bhattarai, D. R. Tiwari, U. Gautam, P. Shrestha, S. Maske, J. Avouac, L. Bollinger, and Pandey M. R. (2013), Double difference relocation of local earthquakes in the Nepal Himalaya, *J. Nepal Geol. Soc.*, *46*, 133–142.

Sapkota, S. N., L. Bollinger, Y. Klinger, P. Tapponnier, Y. Gaudemer, and D. Tiwari (2013), Primary surface ruptures of the great Himalayan earthquakes in 1934 and 1255, *Nat. Geosci.*, *6*, 71–76.

Savage, J. C. (1983), A dislocation model of strain accumulation and release at a subduction zone, *J. Geophys. Res.*, *88*(B6), 4984–4996.

Schiffman, C., B. S. Bali, W. Szeliga, and R. Bilham (2013), Seismic slip deficit in the Kashmir Himalaya from GPS observations, *Geophys. Res. Lett.*, *40*, 5642–5645, doi:10.1002/2013GL057700.

Socquet, A., W. Simons, C. Vigny, R. McCaffrey, C. Subarya, D. Sarsito, B. Ambrosius, and W. Spakman (2006), Microblock rotations and fault coupling in SE Asia triple junction (Sulawesi, Indonesia) from GPS and earthquake slip vector data, *J. Geophys. Res.*, *111*, B08409, doi:10.1029/2005JB003963.

Styron, R., M. Taylor, and K. Okoronkwo (2010), Database of active structures from the Indo-Asian collision, *Eos Trans. AGU*, *91*(20), 181–182, doi:10.1029/2010EO200001.

Thakur, V., M. Joshi, D. Sahoo, N. Suresh, R. Jayangondapermal, and A. Singh (2014), Partitioning of convergence in Northwest Sub-Himalaya: Estimation of late Quaternary uplift and convergence rates across the Kangra Reentrant, north India, *Int. J. Earth Sci.*, *103*(4), 1037–1056, doi:10.1007/s00531-014-1016-7.

Vergne, J., R. Cattin, and J. P. Avouac (2001), On the use of dislocations to model interseismic strain and stress build-up at intracontinental thrust faults, *Geophys. J. Int.*, *147*(1), 155–162, doi:10.1046/j.1365-246X.2001.00524.x.

Vernant, P., R. Bilham, W. Szeliga, D. Drupka, S. Kalita, A. K. Bhattacharyya, V. K. Gaur, P. Pelgay, R. Cattin, and T. Berthet (2014), Clockwise rotation of the Brahmaputra valley relative to India: Tectonic convergence in the Eastern Himalaya, Naga Hills, and Shillong Plateau, *J. Geophys. Res. Solid Earth*, *119*(8), 6558–6571, doi:10.1002/2014JB011196.

Wesnousky, S. G., S. Kumar, R. Mohindra, and V. C. Thakur (1999), Uplift and convergence along the Himalayan Frontal Thrust of India, *Tectonics*, *18*(6), 967–976, doi:10.1029/1999TC900026.